Visualizing formation and dynamics of a three-dimensional sponge-like network of a coacervate in real time

Ryou Kubota[1,*], Taro Hiroi [1,¥], Yuriki Ikuta[1,¥], Yuchong Liu[1,¥], Itaru Hamachi[1,2,*]

[1]Department of Synthetic Chemistry and Biological Chemistry, Graduate School of Engineering, Kyoto University, Katsura, Nishikyo-ku, Kyoto 615-8510, Japan

[2]JST-ERATO, Hamachi Innovative Molecular Technology for Neuroscience, Kyoto University, Katsura, Nishikyo-ku, 615-8530, Japan.

[¥]These authors contributed equally to this work

Correspondence to: rkubota@sbchem.kyoto-u.ac.jp, ihamachi@sbchem.kyoto-u.ac.jp

Abstract

Coacervates, which are formed by liquid–liquid phase separation, have been extensively explored as models for synthetic cells and membraneless organelles, so their in-depth structural analysis is crucial. However, both the inner structure dynamics and formation mechanism of coacervates remain elusive. Herein, we demonstrate real-time confocal observation of a three-dimensional sponge-like network in a dipeptide-based coacervate. *In situ* generation of the dipeptide allowed us to capture the emergence of the sponge-like network via unprecedented membrane folding of vesicle-shaped intermediates. We also visualized dynamic fluctuation of the network, including reversible engagement/disengagement of crosslinks and a stochastic network kissing event. Photo-induced transient formation of a multiphase coacervate was achieved with a thermally responsive phase transition. Our findings expand the fundamental understanding of synthetic coacervates, and provide opportunities to manipulate their physicochemical properties by engineering the inner network for potential applications in development of artificial cells and life-like material fabrication.

Introduction

A coacervate is a condensed fluid that forms by the liquid–liquid phase separation (LLPS) of small organic molecules, polypeptides, pairs of oppositely charged polyelectrolytes, or biomacromolecules in aqueous solution.[1–11] Coacervates are highly dynamic. They exhibit a variety of unique behaviors, including coalescence into larger spherical assemblies upon contact with one another; facilitated chemical reactions upon internal molecular sequestration; and metastability by transforming into solid-like β-sheet fibrils. Owing to their distinctive behavior, coacervates have long been recognized as attractive models for protocells and artificial cells in research into the origins of life.[12–29]

In-depth analysis of the inner structure of a coacervate and its dynamics is essential for understanding synthetic coacervate systems and their application. Therefore, extensive efforts have been made in this field. Cryogenic transmission/scanning electron microscopy (cryo-TEM/SEM) has been used to visualize three-dimensional (3D) sponge-like bicontinuous networks, which are composed of condensed molecules and aqueous phases, and constitute the inner structures of a wide range of synthetic coacervates.[30–38] In 1990, Bassereau *et al.* reported a randomly connected bilayer network in a coacervate composed of cetylpyridinium chloride and 1-hexanol by freeze-fracture electron microscopy (EM).[31] Kataoka, Kishimura *et al.* demonstrated TEM tomographic images of the 3D connected network comprising unilamellar membranes in a polyethylene glycol (PEG)-

modified polyelectrolyte complex fixed with glutaraldehyde.[35] These 3D sponge-like network structures may be consistent with structural density fluctuation detected by small-angle X-ray/neutron scattering measurements, by which the averaged mesh size was estimated to be 1–100 nm.[39–44] It has been proposed that the sponge-like network structure of synthetic coacervates is related to their unique physical properties, such as low interfacial tension and low cohesive energy.[30] However, EM inevitably requires drying, freezing, and/or fixation for sample preparation, so that only static images of the specimens can be illustrated, and dynamic information about the sponge-like network is not clearly addressed. Even using the rapidly developing liquid-phase TEM technique, researchers have not been able to obtain clear images of the sponge-like coacervate network in real time.[45,46] Although time-lapse observation of coacervates is widely conducted by widefield and confocal microscopy,[47] to date these light-based imaging techniques have visualized only homogeneous structures of coacervates, but not yet sponge-like morphologies. Investigations of the inner dynamics of coacervates rely heavily on fluorescence recovery after photobleaching (FRAP) and/or fluorescence correlation spectroscopy (FCS) analyses, which only provide the diffusion coefficients of fluorescently labeled components. Moreover, it is generally considered that coacervates form through nucleation or spinodal decomposition.[48–51] The formation mechanism of a sponge-like morphology has never been examined by microscopic or spectroscopic methods. Therefore, both the inner structure dynamics and the formation mechanism of 3D sponge-like networks remain elusive.

Herein, we describe real-time imaging of the generation and dynamics of a 3D sponge-like network in a dipeptide-based coacervate by confocal-based super-resolution microscopy (Fig. 1a). A diphenylalanine peptide modified with a *tert*-butyl ester at the *C*-terminus (FF-OtBu; F = L-phenylalanine) was recently developed as a novel structural motif for LLPS.[52] To examine its formation process in real time, we designed a reaction for *in situ* generation of PEG_9-FF-OtBu, in which two distinct phenylalanine fragments were linked to yield a coacervate-forming dipeptide (Fig. 1b). Time-lapse imaging reveals the emergence of a 3D sponge-like network in a coacervate, which proceeds through the unexpected membrane folding of vesicle-shaped intermediates. The resulting interpenetrated network exhibits dynamic structural fluctuation, which has not yet been investigated by EM; i.e., the spontaneous engagement and disengagement of network crosslinks, and a stochastic kissing event between the outer networks of different coacervate droplets before fusion. Furthermore, we succeeded in demonstrating a pathway-dependent thermally responsive phase transition, in which the intermediate states differed depending on temperature. The transient generation of a multiphase coacervate can also be achieved by the local irradiation of gold

nanoparticles encapsulated in a coacervate with a laser.

Results

Real-time imaging of the coacervate formation process via *in situ* synthesis

We recently discovered a structurally simple FF-OtBu motif for LLPS. We employed an FF dipeptide that has widely been used in a field of supramolecular soft materials because of its self-assembly ability for β-sheet type nanofibers/hydrogels and nanotubes through hydrogen-bonding and π–π interactions in aqueous solutions.[53–61] The FF dipeptide was modified with a bulky *t*-Bu group at the *C*-terminus to suppress the formation of supramolecular nanofibers via steric hindrance (Fig. S1). Our objective was to induce LLPS. We demonstrated that the resultant coacervate enabled molecular sequestration and facilitated internal reactions.[52] In the present study, we generated an FF-OtBu motif by condensing an *N*-terminus-modified phenylalanine (*N*-modified F-OH) and a phenylalaninate *tert*-butyl ester (H-F-OtBu) *in situ* in an aqueous buffer solution to investigate the formation of a coacervate in real time (Fig. 2a). It was expected that as the reaction progressed, the concentration of the *N*-terminus-modified FF-OtBu derivative would gradually increase and exceed the critical concentration, thereby enabling the aggregate formation process to be observed *in situ* in real time. We used a phenylalanine derivative modified with a hydrophilic nonaethylene glycol group at the *N*-terminus (PEG_9-F-OH). DMT-MM (4-(4,6-dimethoxy-1,3,5-triazin-2-yl)-4-methylmorpholinium chloride) was selected as a condensation reagent because of the higher reactivity under mild aqueous conditions than 1-ethyl-3-(3-dimethylaminopropyl)carbodiimide (EDC; another water-soluble condensation reagent) and its water-soluble side-products that may not interfere with self-assembly.[62] The reaction was initiated by adding a buffer solution comprising DMT-MM to a mixture of PEG_9-F-OH and H-F-OtBu, and incubating the mixture at 25 °C. The transmittance gradually decreased as the reaction proceeded, indicating that certain self-assemblies had formed (Fig. S2). Reverse-phase high-performance liquid chromatography (RP-HPLC) analysis of the reaction mixture confirmed the formation of the desired product, i.e., PEG_9-FF-OtBu (Fig. S3).

We next monitored the formation of self-assemblies comprising PEG_9-FF-OtBu by confocal-based super-resolution Airyscan imaging in real time. We used a hydrophobic rhodamine 6G (rho6G) dye as a fluorescent probe (Fig. S1). Time-lapse imaging revealed the unique formation of coacervate droplets via the membrane folding of vesicle-like assemblies as key intermediates (Fig. 2b, Movie S1). No structures were observed during the initial stage of the reaction. However, after 15 min, many small puncta with diameters of less than 1 μm emerged. These puncta exhibited Brownian movement and gradually grew into larger distorted vesicle-like assemblies with diameters of 3–5 μm (they resembled ring-like structures in *xy* slice images: see Fig. 2c and Fig. S4 for a *z*-

stack 3D image). The membrane comprised two thin-layer structures that thermally fluctuated, as confirmed by line plot analysis (Fig. S5). These vesicle-like assemblies increased in size (typically to more than 10 μm in diameter), mainly by fusing with each other, then transformed into coacervate droplets via unique dynamic structural changes. As shown in Fig. 2d, three small vesicle-like assemblies (diameters: 3, 3.5, and 5 μm) touched each other to form larger distorted assemblies with several crosslinking points (longest diameter: approximately 10 μm). The resultant assemblies frequently transformed into various shapes with crosslinking points that dynamically engaged and disengaged (indicated by yellow and blue arrows in Fig. 2d, respectively). Subsequently, numerous crosslinking points spontaneously formed at the centers of the self-assemblies, and the swaying outer edge of the membrane was gradually incorporated into the core with forming new crosslinking points, resulting in a distorted spherical assemblage with a complex densely-meshed network (diameter: approximately 6 μm). We term this unique process "membrane folding", and it ended within approximately 6 min. The mesh network of the spherical assemblies rapidly rearranged, and the assemblies coalesced into larger assemblies. The liquid-like property of the resultant assemblies was confirmed by both their fusion event and fluorescence recovery after photobleaching (FRAP) analysis, thus the assemblies are characterized as coacervates (Fig. 2b, S6). To further investigate the *in situ* formation, we performed time-dependent HPLC analyses. The HPLC analysis showed that PEG_9-FF-OtBu increased linearly with reaction time (Fig. S7). Consequently, the concentration of PEG_9-FF-OtBu was estimated to be 0.2 mM at the time vesicle-like assemblies begun to emerge (15 min), which is well consistent with the critical coacervation concentration determined by the use of purified PEG_9-FF-OtBu (see below for detail; Fig. S13). We thus concluded that the vesicle-like assemblies are kinetic intermediates and the coacervate droplets are the thermodynamically-stable product under the *in situ* formation condition. The control experiments confirmed that neither the vesicle-like intermediates nor the coacervate droplets occurred in the absence of PEG_9-F-OH, H-F-OtBu, or DMT-MM, indicating that they comprised PEG_9-FF-OtBu (Fig. S8). We noticed that the observed mesh network resembled the inner self-assembling structure of coacervates previously revealed by cryo-TEM. For the first time, the designed *in situ* generation protocol of the coacervate-forming dipeptide enabled us to observe the formation of a coacervate bearing an inner mesh network by time-lapse Airyscan imaging.

Using this simple system, we examined the dependence of coacervate formation on amino acids by utilizing various *t*Bu esters of aromatic, hydrophobic, and hydrophilic amino acids instead of H-F-OtBu (H-W-OtBu, H-L-OtBu, H-S-OtBu, and H-G-OtBu, Fig. 2a). Time-lapse Airyscan imaging revealed that numerous liquid-like coacervate droplets emerged when using H-W-OtBu

and H-L-OtBu (PEG_9-FW-OtBu and PEG_9-FL-OtBu generation, respectively, Fig. 3a, 3b, Movie S2, Movie S3). In these cases, small μm-sized droplets initially appeared, then increased in size through growth and/or fusion processes (Fig. S9a, S9b). In contrast, in the cases of H-S-OtBu and H-G-OtBu (PEG_9-FS-OtBu and PEG_9-FG-OtBu generation, respectively), a very small number of irregularly shaped aggregates appeared, indicating that the hydrophobic dipeptide core is essential for coacervate formation (Fig. 3c, 3d, Fig. S9c, S9d). RP-HPLC analysis confirmed the formation of the desired dipeptide derivatives in all cases (Fig. S10). Fluorescence intensity analysis of the entire field of view revealed distinct initiation of coacervate formation times of approximately 40 min for PEG_9-FF-OtBu and PEG_9-FW-OtBu and approximately 75 min for PEG_9-FL-OtBu (Fig. 3e). To understand the coacervate formation steps in detail, we also analyzed the time course changes of the cross-sectional areas at single-droplet resolution, as shown in Fig. 3f and 3g. In the case of PEG_9-FL-OtBu, a gradual area increment was observed in addition to a stepwise increment, revealing that these droplets grew through both dipeptide uptake and fusion (Fig. 3g, Fig. S11b). In sharp contrast, the droplet size remained almost constant and increased stochastically in a stepwise manner in the case of PEG_9-FW-OtBu, indicating that coacervate growth proceeded mainly through fusion but not uptake of the dipeptide into droplets (Fig. 3f, Fig. S11a). Moreover, we found that some of the droplets shrank, that is the coacervate areas gradually decreased over time (as indicated by the red and purple lines in Fig. 3f). As shown in Fig. 3h, the shrinkage occurred in droplets when another droplet was nearby. Droplet **1** had an area of 13 μm^2 at 1 h 15 min; it gradually decreased to 5.0 μm^2 at 2 h, whereas droplet **2** located next to droplet **1** gradually increased from 26 to 33 μm^2. Time-lapse imaging suggests that a coacervate-forming dipeptide may have been transferred from droplet **1** to droplet **2**. It is worth noting that the membrane folding of the vesicle-like intermediates were never observed in any of the cases except for PEG_9-FF-OtBu. It suggests that the delicate balance of hydrophobicity/hydrophilicity and the resultant intermolecular interactions between PEG_9-FF-OtBu may be essential for the membrane folding of the vesicle-like intermediates. All the coacervate formations we examined were initiated through nucleation, but the growth processes were diverse depending on the amino acid sequence.

Detailed examination of the PEG_9-FF-OtBu coacervate structure

We subsequently confirmed that the same coacervates were formed using pure PEG_9-FF-OtBu separately synthesized in batches (see organic syntheses in the Supporting Information; Fig. S12). The coacervate droplets were prepared by adding a buffer to PEG_9-FF-OtBu, then ultrasonicating and thermally annealing to obtain a white suspension (Fig. S13, see Methods for detail).

Microscopic examination of the resultant suspension revealed micrometer-sized droplets that fused with each other (Fig. 4h). According to microrheological analysis using the Stokes–Einstein equation, the inner viscosity of the coacervate was approximately 3.68 ± 0.18 Pa·s, which fits within the values of coacervate droplets comprising oppositely-charged polyelectrolytes (typically, between 0.1 and 20 Pa·s depending on the degree of polymerization and charged functional groups)[63] (Fig. S14). We also determined that the critical coacervation concentration was 0.2 mM by transmittance measurements and microscopic observation (Fig. S13, S15). This value is comparable with those of synthetic oppositely-charged polyelectrolyte.[16,37,44] These data revealed that the PEG_9-FF-OtBu formed a liquid-like coacervate.

To investigate the structures and properties of coacervate droplets in detail, we next visualized the inner 3D structures of coacervate droplets by Airyscan. To determine the localization of PEG_9-FF-OtBu, we employed a fluorescent probe, i.e., BODIPY-FF-OtBu, which comprises a BODIPY dye at the *N*-terminus of the FF-OtBu motif (Fig. 1c). As shown in Fig. 4a, 4b, and Movie S4, the coacervate droplets comprised bright, densely-interconnected mesh structures and dark, irregularly shaped and sized voids (pores), which were similar to the structures observed during the *in situ* formation protocol. Line plot analysis revealed the width of the mesh network to be approximately 100–200 nm (Fig. 4c). According to quantitative image analysis, the average size of the voids was 0.03 ± 0.05 μm^2 (Fig. 4d). The *z*-stacked 3D image revealed that the mesh network was interconnected, even in the *z*-direction, forming a 3D sponge-like bicontinuous structure (Fig. 4e, Movie S5). A time-lapse movie revealed that the 3D sponge-like network fluctuated extensively (Movie S4). When the images obtained at different time-points (25.02 and 25.92 s) were overlayed, the networks seemed similar but did not completely overlap with each other (Fig. S16, Movie S6). We carried out FRAP analysis using BODIPY-FF-OtBu as a probe to investigate molecular diffusion inside the sponge-like network. After photobleaching, the fluorescence intensity gradually recovered from the outer edge of the photobleached region over 15 s (Fig. 4f, Fig. S17a, Movie S7). According to exponential fitting analysis, the mobile fraction was 89% ± 3% and the half recovery time was 2.4 ± 0.2 s (Fig. S17b–d). Considering these data and the hydrophobicity of BODIPY-FF-OtBu, the fluorescence probe was able to diffuse within the network. To investigate the chemical properties of the sponge-like network, we determined the uptake of two chemically distinct fluorescent dyes, i.e., fluorescein and rho6G (Fig. S1). The microscope images revealed that hydrophobic rho6G was sequestrated in the network, but hydrophilic fluorescein was not concentrated inside the coacervate (Fig. S18). These uptake behaviors were consistent with the results from quantitative fluorescent spectroscopy analysis (Fig. S19); the uptake tendency differed

from that of the cationic PhePy-FF-OtBu coacervate (Fig. S19c).[52] Therefore, it seems that the sponge-like network provides a hydrophobic environment comprising the FF-OtBu moiety, and the PEG_9 moiety stabilizes the interface between the mesh and the water/buffer-filled voids.

Unique dynamic behavior revealed by real-time imaging

During the real-time imaging experiments, we discovered that the 3D sponge-like coacervate network exhibited dynamic behavior. First, the crosslinks in the network repeatedly engaged and disengaged on a timescale of several tens of milliseconds. We monitored the membrane fluctuation of the coacervate at high spatiotemporal resolution using the Airyscan multiplex mode (16.7 frames per second). As shown in Fig. 4g and Movie S6, the outer and inner membranes were connected to each other to form a crosslinking point until 25.26 s (indicated by the white arrow). The crosslinking point was then cleaved from 25.50 to 26.28 s, followed by recovery after 26.52 s. The stochastic engagement and disengagement of the coacervate crosslinks contrast with the static crosslinks of hydrogels, and reflect the liquid-like behavior of coacervates.

Such dynamic behavior of the coacervate crosslinks plays an important role in the fusion process. Indeed, real-time imaging of the fusion process revealed a unique "kissing" event before fusion. Fig. 4h and Movie S8 show that the outer membranes of distinct coacervate droplets touched each other at 1.95 s but they disengaged at 4.55 s, suggesting that this temporal kissing of the coacervate membrane did not induce fusion. From 18.20 s, the same coacervate droplets touched several times. At 21.45 s, the touching area increased, and then the two coacervate droplets started to fuse with each other. Immediately after the fusion process started, the inner mesh structures of the two droplets interacted and mixed. It is clear that the coacervate fusion started stochastically through such temporal contact between the outer mesh structures.

Pathway-dependent thermally responsive phase transition of the coacervate

The inner structure of a coacervate differs depending on the observation temperature (Fig. 5a). It is well known that polymers modified with PEG chains exhibit thermally responsive phase transition through dehydration of the PEG moiety during heating at a critical temperature (the so-called lower critical solution temperature, LCST).[35,64] We made microscopic observations in the higher temperature (HT) phase at 37 °C. Airyscan imaging revealed spherical assemblies with diameters of several μm that exhibited coalescence (Fig. 5b, Fig. S20). Notably, the 3D sponge-like structure observed at 25 °C (the lower temperature (LT) phase) was not visible during the HT phase. FRAP and microrheological analysis revealed liquid-like properties, indicating that PEG_9-FF-OtBu forms

a coacervate even in the HT phase (Fig. S17 and S14, respectively). The critical coacervation concentration at the HT phase was determined to be 0.2 mM by the transmittance measurement, which is comparable to that at the LT phase (Fig. S13, S15). Quantitative analysis revealed differences in the coacervate structures between the HT and LT phases. Line plot analysis confirmed that the fluorescence intensity in a single droplet was almost constant during the HT phase (0.96 ± 0.02; Fig. 5c red, Fig. S21), whereas the intensity varied markedly during the LT phase owing to the 3D sponge-like network structure (0.77 ± 0.09; Fig. 5c blue, Fig. S21). We also noticed that the coacervate shape near a glass surface seemed almost spherical during the HT phase but was highly distorted during the LT phase; the circularity during the HT phase was estimated to be close to one (0.907 ± 0.008), whereas that during the LT phase was 0.70 ± 0.08 (Fig. S22). Furthermore, the coalescence kinetics during the HT phase were much faster than during the LT phase (Fig. 4h, S20). These data suggest that the interfacial tension during the HT phase may be higher than during the LT phase. Therefore, the PEG_9-FF-OtBu exhibited a coacervate-to-coacervate transition in response to temperature change.

To investigate temperature response in detail, we synthesized a series of di-, nona-, and dodecaethylene glycol-tethered dipeptide derivatives (PEG_2-FF-OtBu, PEG_{12}-FF-OtBu, PEG_9-FW-OtBu, and PEG_9-FL-OtBu). A solution of a coacervate with a shorter diethylene glycol-tethered dipeptide derivative (PEG_2-FF-OtBu) did not exhibit the temperature-dependent structural change (Fig. S23, S24). PEG_{12}-FF-OtBu exhibited an LCST-like monomer-to-coacervate transition at 38 °C to form homogeneous coacervate droplets at the HT phase (Fig. S25, S26, S27, Movie S9, S10). PEG_9-FW-OtBu self-assembled into homogeneous coacervate droplets at 25 °C, but they showed negligible response against temperature until 70 °C (Fig. S28, S29, S30). PEG_9-FL-OtBu showed two-step UCST-LCST-like response at 28 and 40 °C, respectively (Fig. S31, S32). Below 28 °C and above 40 °C, PEG_9-FL-OtBu formed coacervate droplets with a homogeneous structure (Fig. S33). At the middle-temperature phase, a multi-layered membrane-like structure emerged and it never transformed into coacervate droplets. Taken together, both the nonaethylene glycol group and the FF core are essential for thermally responsive phase transition between sponge-like and homogeneous coacervate structures, while the temperature dependent behaviors/morphologies of the different PEG chain length and/or dipeptide core were varied.

We subsequently attempted *in situ* time-lapse imaging of the thermally responsive coacervate-to-coacervate transition in detail. First, we observed the structural transformation from the LT phase to the HT phase induced by heating (Fig. 5d, Movie S11; the sample appears to move because the focus plane drifted owing to the temperature change). After 3 min, the thin-layer membrane

structures budded at the periphery of the coacervate (width: approximately 250–300 nm, Fig. 5e, 5f, Fig. S34). Concurrently, the darker regions stochastically appeared inside the coacervate. During incubation at 37 °C, the inner darker regions grew and fused with each other, and ultimately moved to the edge of the coacervate droplet. Simultaneously, the inner structure became homogeneous and the fluorescence intensity of the coacervate phase increased, probably owing to an increment of quantum yield (Fig. S35). This phase transition behavior proceeded rapidly (within 5 min). After further incubation, the membranes suddenly burst producing numerous spherical coacervates. It was not possible to stain the interiors of the budded thin-layer membranes and inner-separated regions with BODIPY-FF-OtBu, suggesting that their interiors were filled with water/buffer (thus, the inner darker regions can be ascribed to vacuoles[23,51,65–71]). Temperature-dependent phase transition was also confirmed in the bulk state (Fig. S13, S36). Given the temperature-responsive dehydration of the PEG chain, it is reasonable to suppose that the formation of the budded membranes and the inner vacuoles was induced by phase separation due to water release from the PEG_9 chain.

Interestingly, the phase transition from the HT to the LT phase proceeded through a different intermediate state (Fig. 5g, Movie S12). After setting the temperature controller to cool from 37 to 25 °C, the coacervate droplets coalesced and the fluorescence intensity gradually and simultaneously decreased. After 30 min, the inner sponge-like network appeared without the budded membranes and the dark vacuoles inside the coacervates. The overall changes were completed within approximately 60 min. Compared with the LT-to-HT phase transition, the HT-to-LT phase took much longer to reach a thermally equilibrated state, probably because of slow water/buffer uptake into the coacervate droplets for the hydration of the PEG_9 chain. This may have been the main reason the PEG_9-FF-OtBu coacervates exhibited pathway-dependent phase transition behavior.

Photo-induced transient phase separation inside a coacervate containing gold nanoparticles

Encouraged by the temperature-responsive coacervate-to-coacervate transition, we manipulated the inner structure of a coacervate by exploiting the photothermal effect of gold nanoparticles (AuNPs).[16,72] It is reasonable to suppose that thermally induced coacervate-to-coacervate transition can be triggered by local heat generation induced by irradiating AuNPs trapped in the coacervate with light (Fig. 6a). A solution containing AuNPs with diameters of 100 nm was added to the coacervate solution, and the resultant mixture was incubated at 37 °C for 15 min, then at 25 °C for 1 h. A widefield microscope image revealed that the AuNPs were entrapped inside the coacervate (Fig. 6b). We then locally irradiated the entrapped AuNPs for 7.3 s with intense laser light (561 nm)

using a FRAP experiment setup, and monitored time-dependent changes. Immediately after light irradiation, a higher fluorescence region with a diameter of approximately 4 μm appeared around the irradiated region (Fig. 6c, 6d, Movie S13). The 3D sponge-like structure was not visible in this region, so the higher fluorescence region can be assigned to the HT phase. Subsequently, the HT phase region gradually broadened and the boundary between the LT phase became unclear. After approximately 70 s, the HT phase region completely disappeared. Concurrently, thin layer-like membranes similar to those observed during the LT-to-HT phase transition budded at the periphery of the coacervate, suggesting that water/buffer was expelled from the temporal HT region owing to dehydration of the PEG_9 chain. According to the quantitative analysis of the fluorescence intensity, the half-life of the temporal HT region was approximately 26.0 ± 0.4 s (Fig. 6e). The coacervate diameter transiently decreased immediately after laser irradiation, and started to increase after 40 s (Fig. 6f). A control experiment confirmed that such local phase separation did not occur when the AuNPs-free area was irradiated with 561 nm laser radiation (Fig. S37). These results indicate that the structures and properties of a PEG_9-FF-OtBu coacervate can be spatiotemporally controlled by combining it with functional nanoparticles.

Discussion

The results presented herein demonstrate that 3D sponge-like inner/interfacial networks are remarkably dynamic in coacervate droplets. Although cryo-TEM/SEM have been used to characterized sponge-like networks as the inner self-assembling structures of coacervates, these EM-based observation techniques can only provide static structural information owing to sample freezing and/or fixation. FRAP and FCS analyses only provide the diffusion coefficients of fluorescently labeled components, not the inner dynamics of coacervates. In contrast, our real-time imaging study revealed various types of fluctuation of the sponge-like network, including reversible crosslinking formation and stochastic membrane kissing. Moreover, we succeeded in observing the formation of these 3D sponge-like networks, which involves an unprecedented membrane folding step of the intermediate vesicle-shaped assemblies. This observation is consistent with an earlier report on the structural transformation of a small molecule-surfactant system from a shear-induced metastable L_α phase (multilamellar) to a thermally equilibrated L_3 phase (coacervate) confirmed by a single snapshot obtained using freeze fracture EM.[32] The similar coacervate-to-vesicle morphological transformation depending on concentration and environmental conditions (e.g., temperature and salt concentration) was also observed in a pair of oppositely charged synthetic polyelectrolytes[73], recombinant protein complexes fused with elastin-like polypeptides[74,75], and

RNA–protein complexes[65], in which dynamics of the inner self-assembled structures were not visualized. Our structure-dependent data demonstrated that solely PEG_9-FF-OtBu exhibits the membrane folding of the vesicular intermediates, the sponge-like network of coacervates, and thermally-responsive coacervate-to-coacervate transition, implying the significance of intermolecular interactions derived from delicate balance of hydrophilicity/hydrophobicity. These results thus provide a better understanding of the structure–property relationships of coacervates, and deliver valuable insights into synthetic LLPS, whose formation mechanism remains poorly understood.

We also achieved the photo-induced generation of a multiphase coacervate using encapsulated AuNPs. Multiphase coacervates have received considerable attention because they are involved in myriad essential biological processes.[76–78] Inspired by these biological events, a few synthetic multiphase LLPS materials have been developed by careful combination of different coacervates with distinct physicochemical properties (e.g., interfacial tension).[52,63,70,79–85] Our multiphase coacervate system is similar to these previous researches; interfacial tension of the inner HT phase is higher than that of the outer LT phase. However, transient multiphase coacervation is carried out in a different manner, i.e., the *in situ* generation of distinct coacervate phases consisting of a single dipeptide derivative by integration of its thermally induced response and the photothermal effect of AuNPs. Such stimulus-triggered control of the sponge-like network in terms of mesh size and dynamics could provide a new way of manipulating the liquid-like properties of synthetic LLPS materials. Our droplet engineering will facilitate the development of evolvable artificial cells by controlled growth and division in the near future.

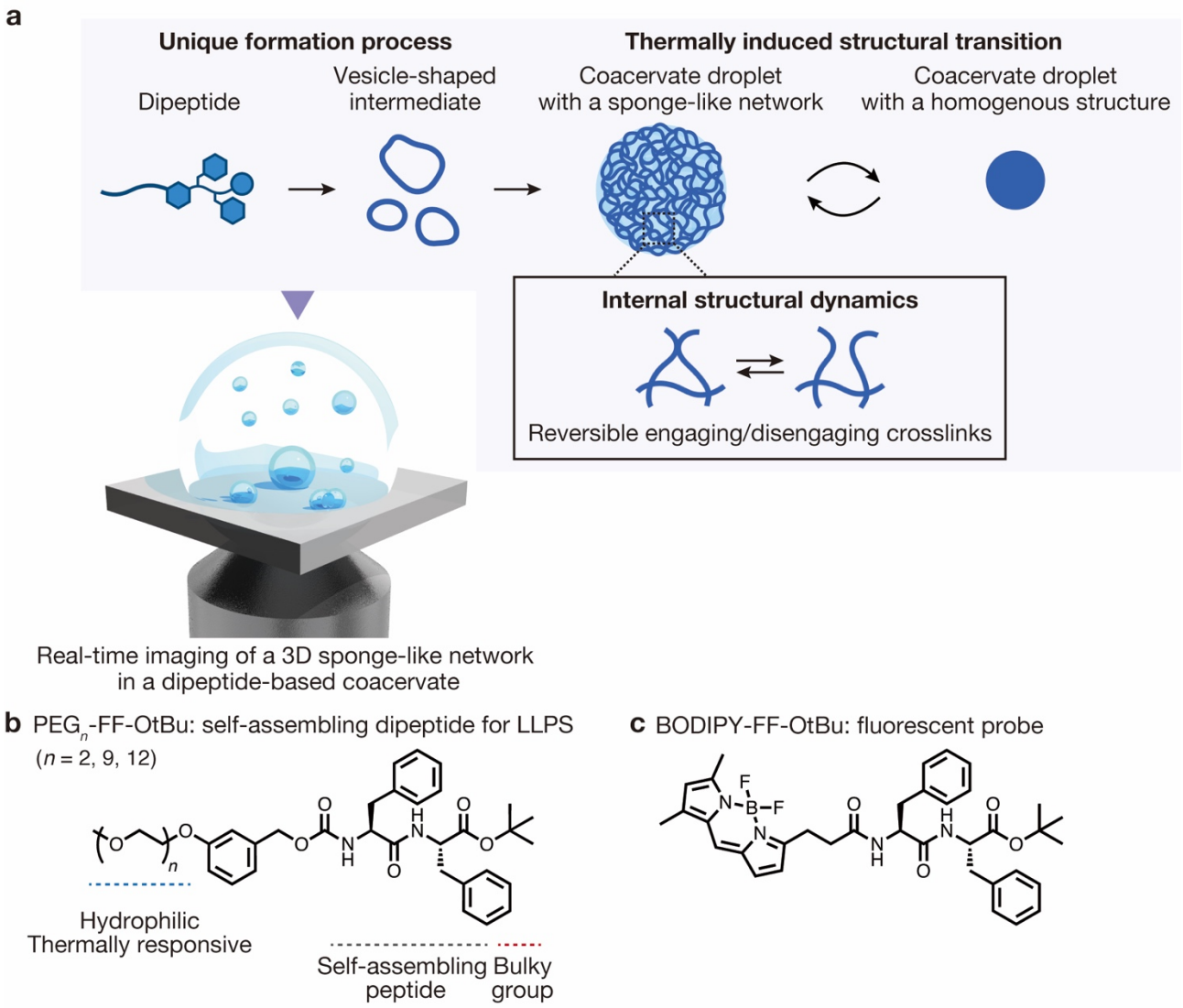

Fig. 1. Conceptual illustration of this research. (**a**) Schematic illustration of real-time confocal imaging of formation and dynamics of a three-dimensional (3D) sponge-like network in a dipeptide-based coacervate. (**b**,**c**) Chemical structures of (**b**) a self-assembling dipeptide derivative for liquid–liquid phase separation (LLPS), PEG$_n$-FF-OtBu (n = 2, 9, 12), and (**c**) a fluorescent probe, BODIPY-FF-OtBu. Other molecules used in this study are shown in Fig. S1.

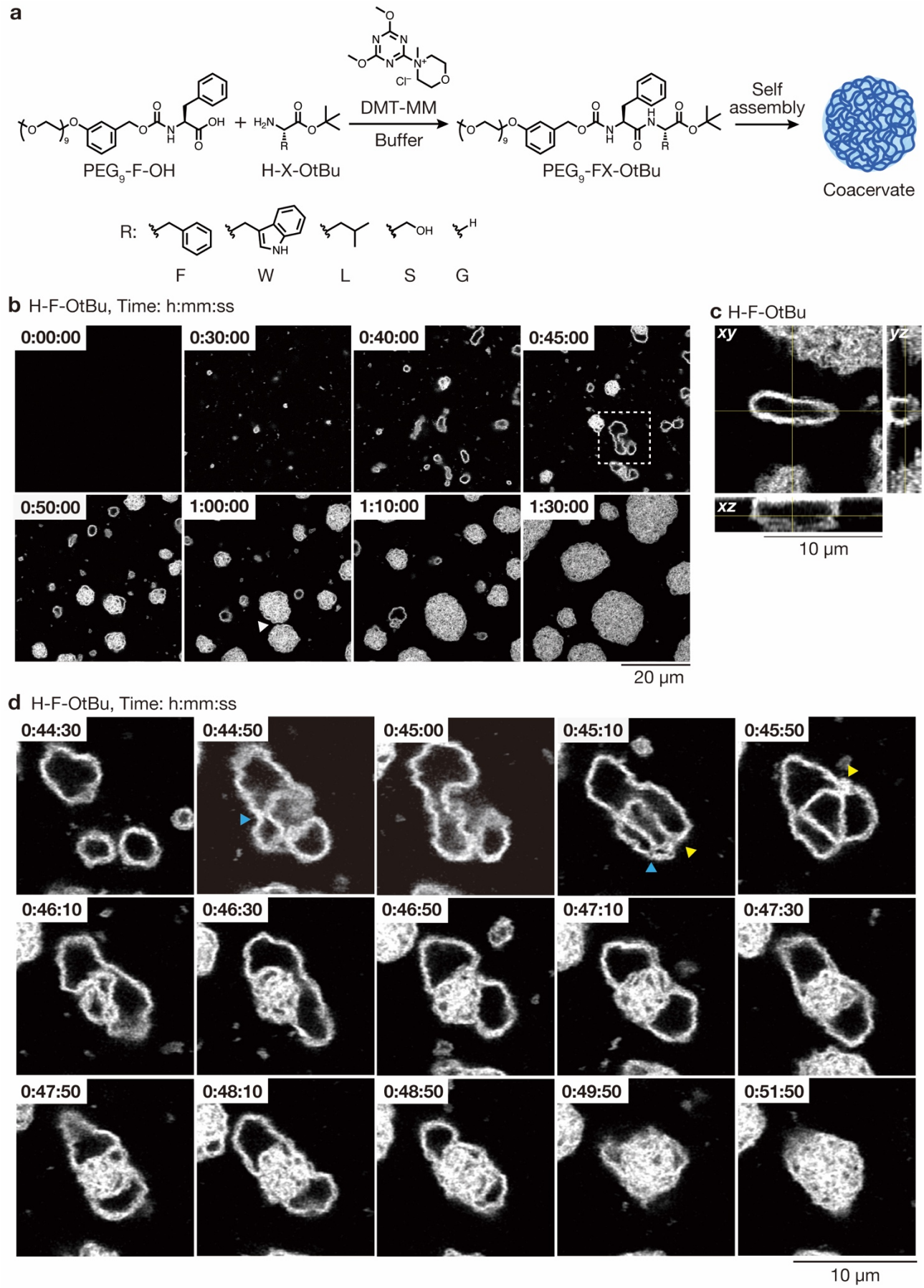
a
DMT-MM
Buffer
Self assembly
PEG9-F-OH
H-X-OtBu
PEG9-FX-OtBu
Coacervate
R:
F
W
L
S
G
b H-F-OtBu, Time: h:mm:ss
0:00:00
0:30:00
0:40:00
0:45:00
0:50:00
1:00:00
1:10:00
1:30:00
20 µm
c H-F-OtBu
xy
yz
xz
10 µm
d H-F-OtBu, Time: h:mm:ss
0:44:30
0:44:50
0:45:00
0:45:10
0:45:50
0:46:10
0:46:30
0:46:50
0:47:10
0:47:30
0:47:50
0:48:10
0:48:50
0:49:50
0:51:50
10 µm

Fig. 2. Real-time Airyscan imaging of formation of the 3D sponge-like network. (**a**) Scheme for a reaction for *in situ* generation of the dipeptide derivatives by condensation between PEG_9-F-OH and H-X-OtBu in the presence of DMT-MM. (**b**) Real-time confocal images of the formation process of PEG_9-FF-OtBu coacervates. A white arrow highlights a point of coacervate fusion. (**c**) 3D imaging of an intermediate vesicle-like assembly. (**d**) Magnified images of the fusion and membrane folding process of vesicle-like assemblies into a coacervate droplet. Blue and yellow arrows highlight points of crosslink cleavage and formation, respectively. Condition: [PEG_9-F-OH] = [H-F-OtBu] = [DMT-MM] = 10 mM, [rhodamine 6G] = 10 μM, 50 mM MES, pH 7.0, 25 °C. DMT-MM: 4-(4,6-Dimethoxy-1,3,5-triazin-2-yl)-4-methylmorpholinium chloride. All samples shown in this figure were prepared by the *in situ* condensation reaction.

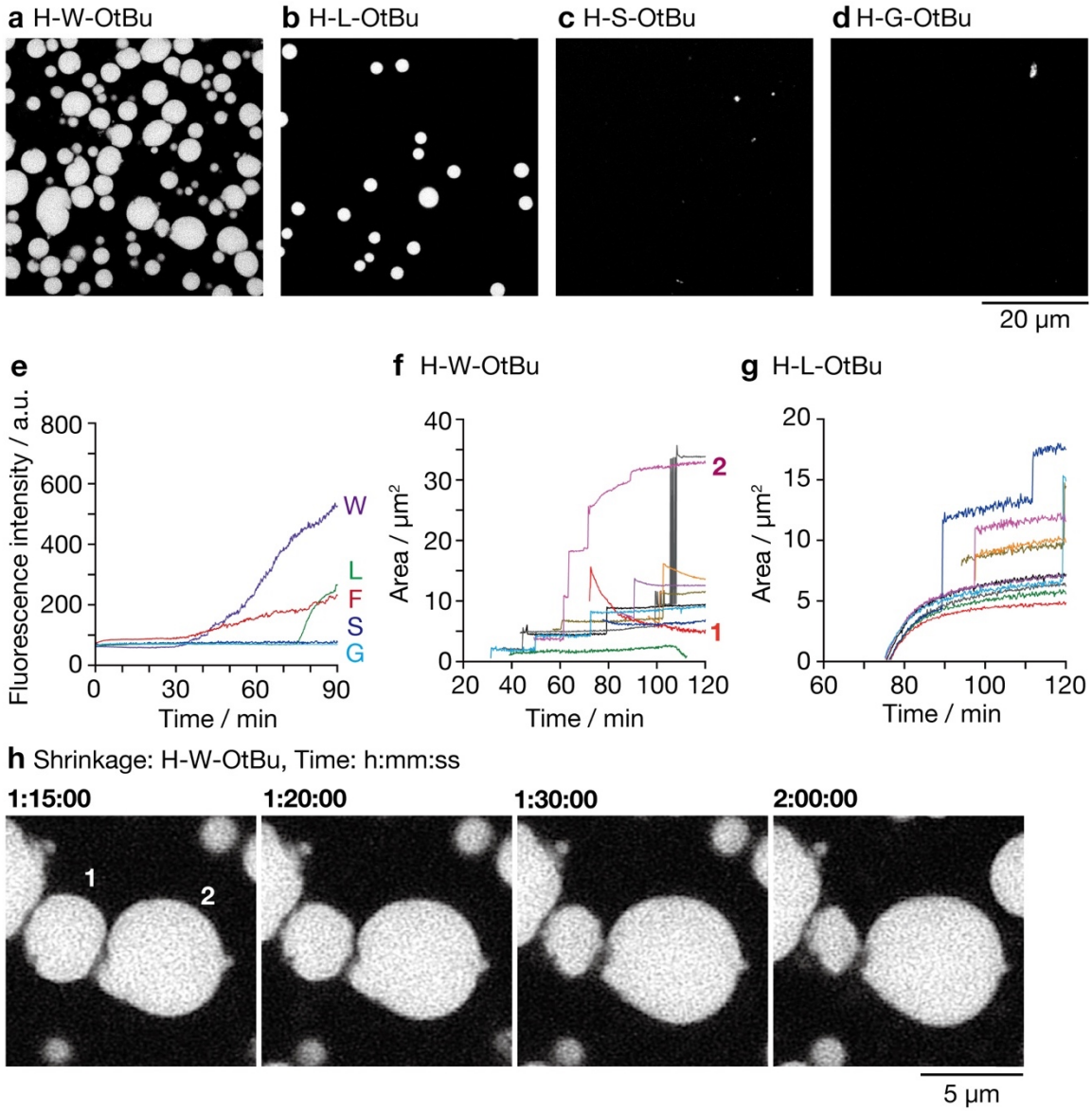

Fig. 3. Dependence of coacervate formation on the dipeptide core. (**a**–**d**) Airyscan images 1.5 h after reaction of PEG_9-F-OH and (**a**) H-W-OtBu, (**b**) H-L-OtBu, (**c**) H-S-OtBu, or (**d**) H-G-OtBu in the presence of DMT-MM. (**e**) Time course of fluorescence intensity changes during reaction of PEG_9-F-OH and (red) H-F-OtBu, (purple) H-W-OtBu, (green) H-L-OtBu, (blue) H-S-OtBu, or (light blue) H-G-OtBu. (**f**,**g**) Time course changes of cross-sectional areas during reaction of PEG_9-F-OH and (**f**) H-W-OtBu and (**g**) H-L-OtBu (n = 10). Regions of interest are shown in Fig. S11. (**h**) Shrinkage of coacervate droplets when using H-W-OtBu. Condition: [PEG_9-F-OH] = [H-X-OtBu] = [DMT-MM] = 10 mM, [rhodamine 6G] = 10 μM, 50 mM MES, pH 7.0, 25 °C. All samples shown in this figure were prepared by the *in situ* condensation reaction.

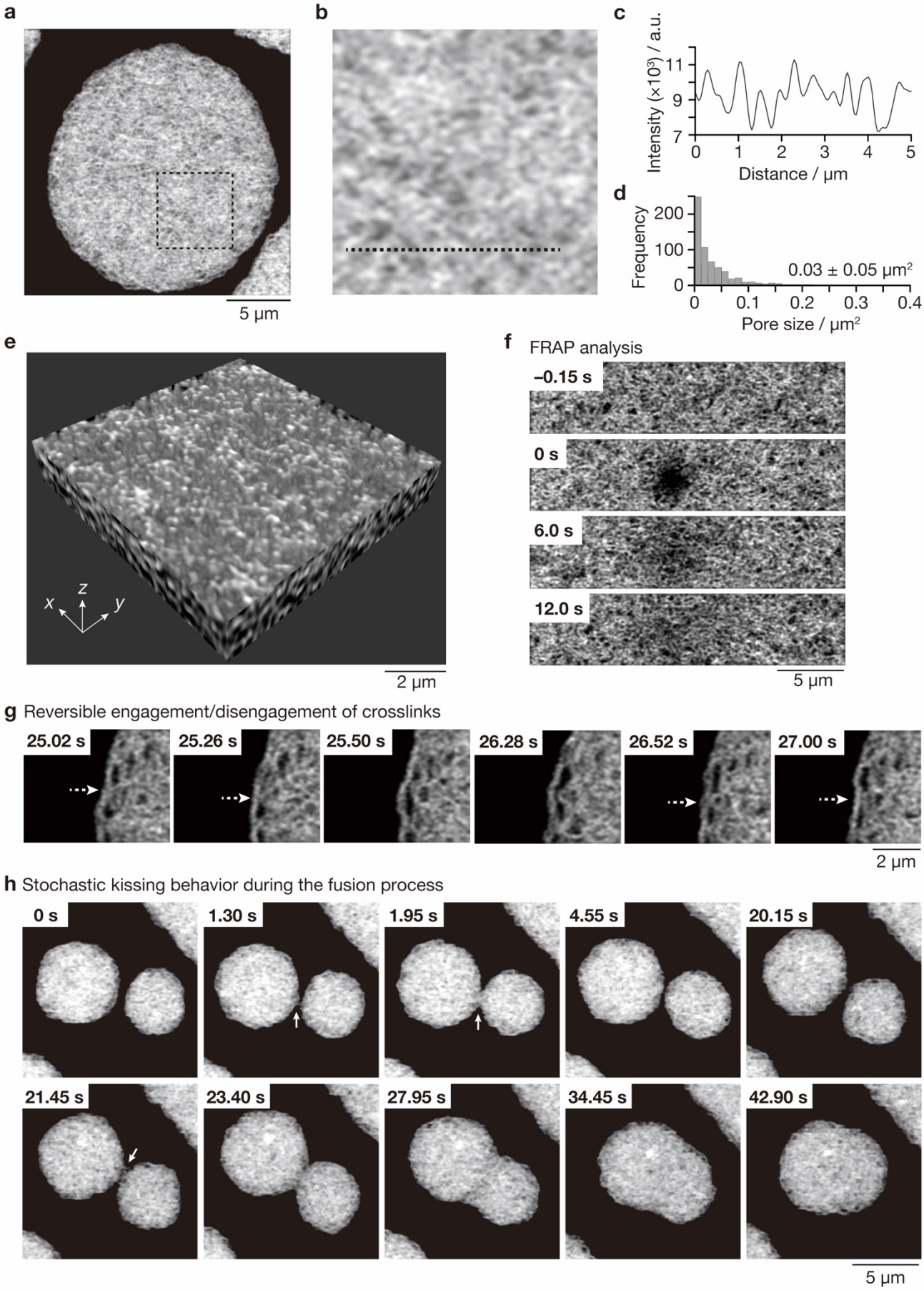

Fig. 4. Structure and dynamics of the sponge-like network in the coacervate. (**a**) Airyscan image of

a PEG_9-FF-OtBu coacervate. (**b**) Magnified image of a black square shown in Fig. 4a. (**c**) Line plot analysis of fluorescence intensity along a black line shown in Fig. 4b. (**d**) Distribution of the estimated pore size in the coacervate. The data represent the mean ± s.d. (n = 750). (**e**) 3D Airyscan image of a PEG_9-FF-OtBu coacervate. A partial structure was shown. (**f**) Time-lapse images of FRAP analysis. (**g**) Reversible crosslink engagement and disengagement in the sponge-like network. Crosslinking points are highlighted by white arrows. (**h**) Stochastic kissing behavior during a coacervate fusion process. Kissing points are highlighted by white arrows. Condition: [PEG_9-FF-OtBu] = 1.0 mM, [BODIPY-FF-OtBu] = 10 μM, 50 mM MES, pH 7.0, 25 °C. All samples shown in this figure were prepared by the ultrasonication method with pure PEG_9-FF-OtBu.

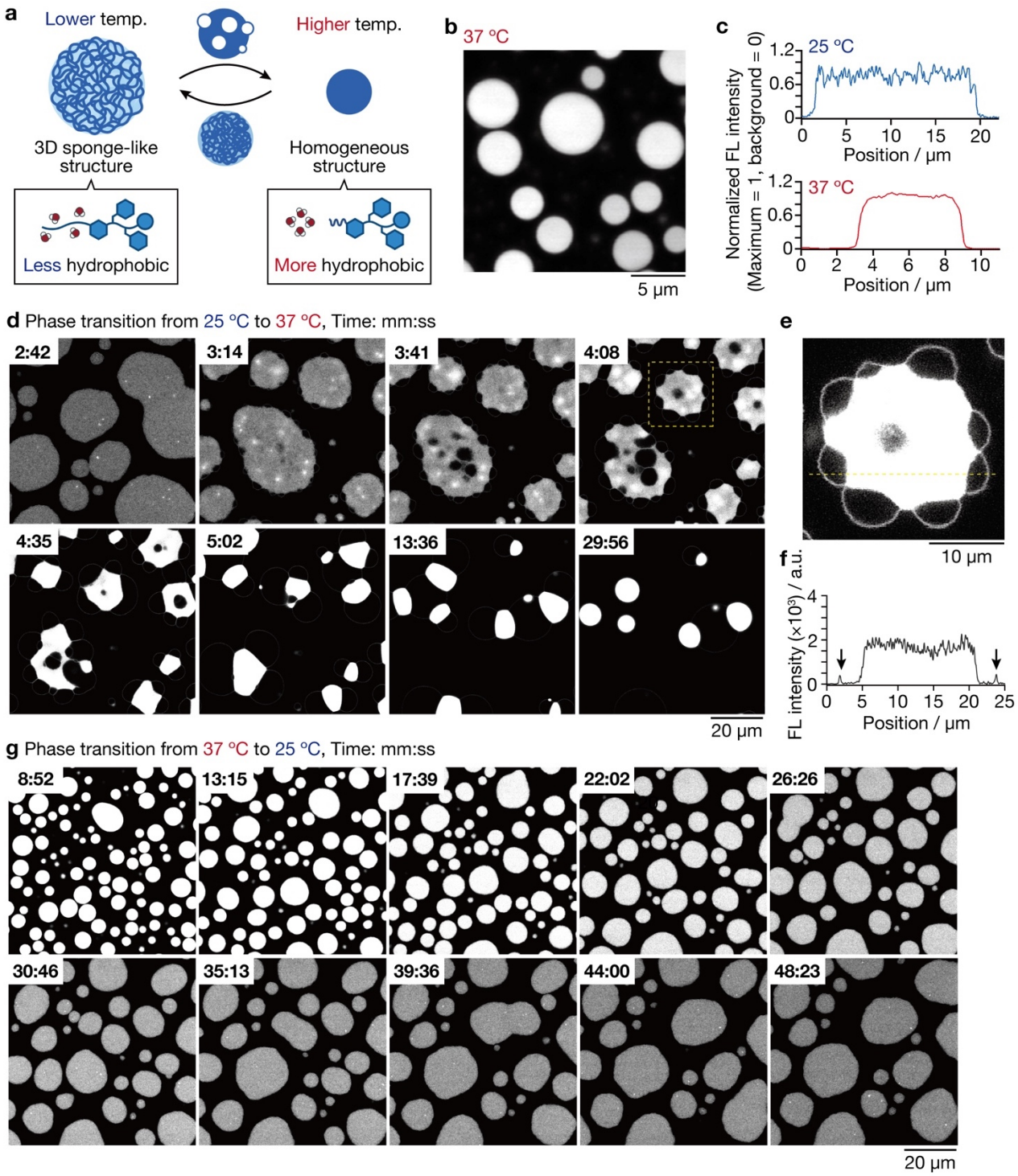

Fig. 5. Pathway-dependent thermally responsive phase transition of the coacervate. (**a**) Schematic illustration of thermally responsive phase transition of the PEG_9-FF-OtBu coacervate. (**b**) Airyscan image of PEG_9-FF-OtBu coacervates at 37 °C. (**c**) Line plot analysis of the normalized fluorescence intensity at (top) 25 and (bottom) 37 °C. Regions of interest are shown in Fig. S21. (**d**,**g**) Time-lapse imaging of thermally responsive structural changes of the coacervates (**d**) from 25 to 37 °C and (**g**) from 37 to 25 °C. (**e**) The magnified image of a budding coacervate highlighted by a yellow square in Fig. 5d. The contrast is enhanced to highlight thin-layer membrane structures. (**f**) Line plot

analysis of fluorescence (FL) intensity along a yellow line shown in Fig. 5e. Black arrows highlight fluorescence intensity of thin-layer membranes. The temperature dependent phase transition was also examined at the bulk state (Fig. S13, S15, S36). Condition: [PEG_9-FF-OtBu] = 1.0 mM, [BODIPY-FF-OtBu] = 10 μM, 50 mM MES, pH 7.0, 25 or 37 °C. All samples shown in this figure were prepared by the ultrasonication method with pure PEG_9-FF-OtBu.

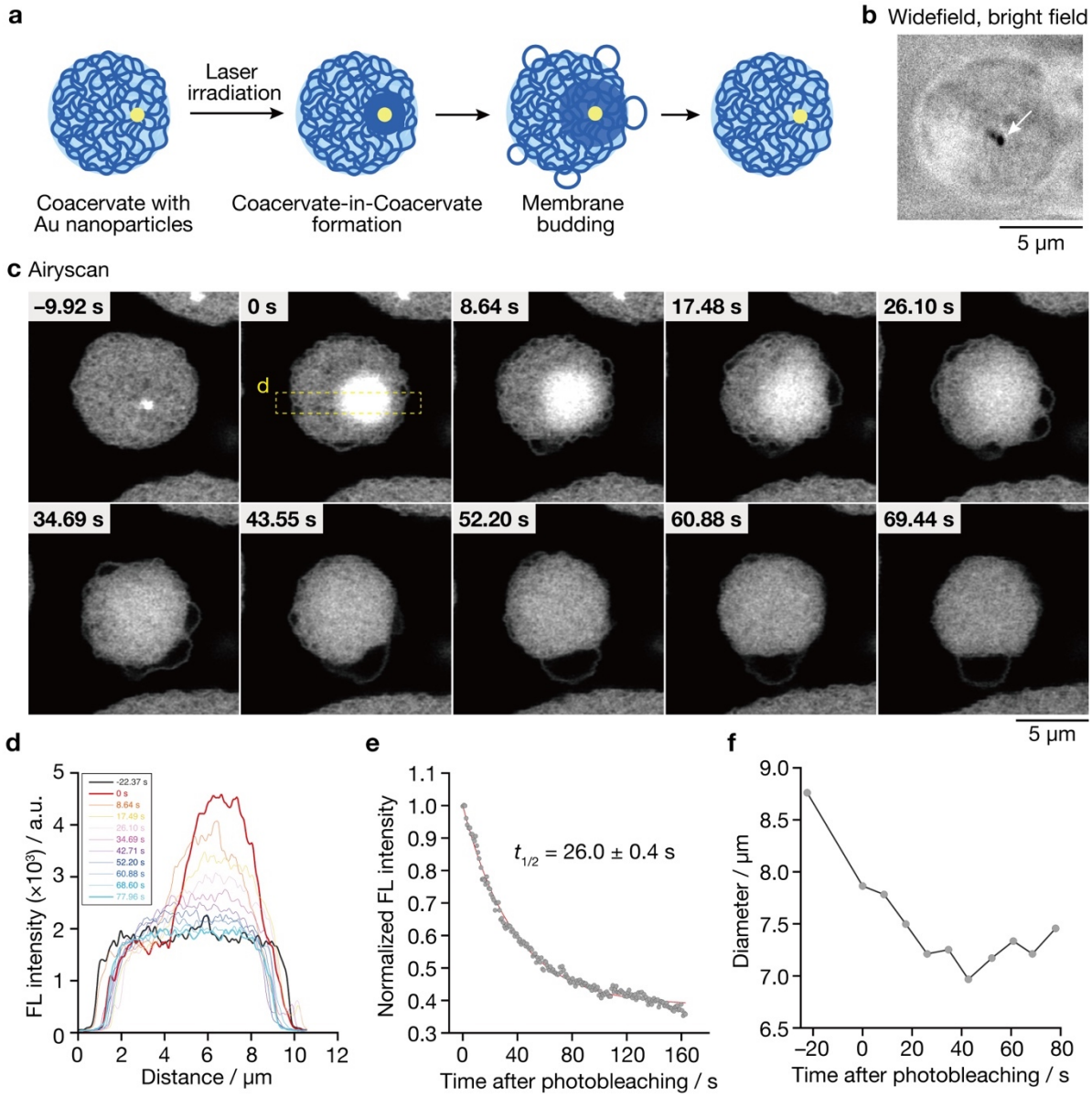

Fig. 6. Photo-induced transient generation of a multiphase coacervate containing gold nanoparticles (AuNPs). (**a**) Schematic illustration of photo-induced coacervate manipulation using AuNPs. (**b**) Widefield microscopic image of a coacervate containing AuNPs (highlighted by a white arrow). (**c**) Time-lapse Airyscan imaging of a coacervate containing AuNPs before and after laser irradiation. Time just after laser irradiation set at 0 s. The fluorescent probe, BODIPY-FF-OtBu, does not show any absorbance at 561 nm, so that no photobleaching occurred when an Au nanoparticle was irradiated with 561 nm laser (Fig. S38). (**d**) Line plot analysis of fluorescence intensity along a yellow rectangle shown in Fig. 6c. (**e**,**f**) Time course changes of (**e**) fluorescence intensity of the irradiated area and (**f**) the coacervate diameter before and after laser irradiation. Condition: [PEG_9-FF-OtBu] = 1.0 mM, [BODIPY-FF-OtBu] = 10 μM, 50 mM MES, pH 7.0, 25 °C. All samples shown in this figure were prepared by the ultrasonication method with pure PEG_9-FF-OtBu.

Associated content

Supporting information

The Supporting information is available free of charge at https://pubs.acs.org/doi/10.1021/jacs.XXXXXX.

Description of materials, experimental methods, organic syntheses, and compound characterization; chemical structures of the fluorescent probes; time-dependent transmittance measurement, HPLC analyses, and microscopic observation of *in situ* condensation reaction; line plot analyses of microscopic images; determination of critical coacervation concentration; microrheological analysis; FRAP analysis; fluorescent dye uptake; temperature-dependent transmittance measurement; negative control results of laser irradiation to coacervate droplet containing Au nanoparticles (PDF).

Time-lapse Airyscan movie of *in situ* formation of the coacervates with H-F-OtBu (the same as Fig. 2b). Condition: [PEG_9-F-OH] = [H-F-OtBu] = [DMT-MM] = 10 mM, [rhodamine 6G] = 10 μM, 50 mM MES, pH 7.0, 25 °C. Elapsed time was displayed as hh:mm:ss (MP4).

Time-lapse Airyscan movie of *in situ* formation of the coacervates with H-W-OtBu (the same as Fig. S9a). Condition: [PEG_9-F-OH] = [H-W-OtBu] = [DMT-MM] = 10 mM, [rhodamine 6G] = 10 μM, 50 mM MES, pH 7.0, 25 °C. Elapsed time was displayed as hh:mm:ss (MP4).

Time-lapse Airyscan movie of *in situ* formation of the coacervates with H-L-OtBu (the same as Fig. S9b). Condition: [PEG_9-F-OH] = [H-L-OtBu] = [DMT-MM] = 10 mM, [rhodamine 6G] = 10 μM, 50 mM MES, pH 7.0, 25 °C. Elapsed time was displayed as hh:mm:ss (MP4).

Time-lapse Airyscan movie of structural fluctuation of the sponge-like network of PEG_9-FF-OtBu. Condition: [PEG_9-FF-OtBu] = 1.0 mM, [BODIPY-FF-OtBu] = 10 μM, 50 mM MES, pH 7.0, 25 °C. Elapsed time was displayed as sec (MP4).

3D Airyscan image of the sponge-like network of PEG_9-FF-OtBu (the same as Fig. 4e). Condition: [PEG_9-FF-OtBu] = 1.0 mM, [BODIPY-FF-OtBu] = 10 μM, 50 mM MES, pH 7.0, 25 °C (MP4).

Time-lapse movie of structural fluctuation of the sponge-like network of PEG_9-FF-OtBu with the

Airyscan multiplex mode (the same as Fig. 4g). Condition: [PEG_9-FF-OtBu] = 1.0 mM, [BODIPY-FF-OtBu] = 10 μM, 50 mM MES, pH 7.0, 25 °C. Elapsed time was displayed as sec (MP4).

FRAP analysis of the coacervate (the same as Fig. 4f). Condition: [PEG_9-FF-OtBu] = 1.0 mM, [BODIPY-FF-OtBu] = 10 μM, 50 mM MES, pH 7.0, 25 °C. Elapsed time was displayed as sec (MP4).

Time-lapse movie of the coacervate fusion (the same as Fig. 4h). Condition: [PEG_9-FF-OtBu] = 1.0 mM, [BODIPY-FF-OtBu] = 10 μM, 50 mM MES, pH 7.0, 25 °C. Elapsed time was displayed as sec (MP4).

Time-lapse Airyscan movie of formation of the PEG_{12}-FF-OtBu coacervates (the same as Fig. S27a). Condition: [PEG_{12}-FF-OtBu] = 10 mM, [BODIPY-FF-OtBu] = 10 μM, 50 mM MES, pH 7.0, from 25 to 40 °C. Elapsed time was displayed as sec (MP4).

Time-lapse Airyscan movie of decomposition of the PEG_{12}-FF-OtBu coacervates (the same as Fig. S27b). Condition: [PEG_{12}-FF-OtBu] = 10 mM, [BODIPY-FF-OtBu] = 10 μM, 50 mM MES, pH 7.0, from 40 to 25 °C. Elapsed time was displayed as sec (MP4).

Time-lapse Airyscan movie of phase transition of the coacervate from 25 °C to 37 °C (the same as Fig. 5d). Condition: [PEG_9-FF-OtBu] = 1.0 mM, [BODIPY-FF-OtBu] = 10 μM, 50 mM MES, pH 7.0. Elapsed time was displayed as mm:ss (MP4).

Time-lapse Airyscan movie of phase transition of the coacervate from 37 °C to 25 °C (the same as Fig. 5g). Condition: [PEG_9-FF-OtBu] = 1.0 mM, [BODIPY-FF-OtBu] = 10 μM, 50 mM MES, pH 7.0. Elapsed time was displayed as mm:ss (MP4).

Time-lapse Airyscan movie after laser irradiation to the coacervate containing AuNPs (the same as Fig. 6c). Condition: [PEG_9-FF-OtBu] = 1.0 mM, [BODIPY-FF-OtBu] = 10 μM, 50 mM MES, pH 7.0, 25 °C. Elapsed time was displayed as sec (MP4).

Author information

Corresponding authors

Ryou Kubota –*Department of Synthetic Chemistry and Biological Chemistry, Graduate School of Engineering, Kyoto University, Katsura, Nishikyo-ku, Kyoto 615-8510, Japan;* orcid.org/0000-0001-8112-8169; Email: rkubota@sbchem.kyoto-u.ac.jp

Itaru Hamachi – *Department of Synthetic Chemistry and Biological Chemistry, Graduate School of Engineering, Kyoto University, Katsura, Nishikyo-ku, Kyoto 615-8510, Japan; JST-ERATO, Hamachi Innovative Molecular Technology for Neuroscience, Nishikyo-ku, Kyoto 615-8530, Japan;* orcid.org/0000-0002-3327-3916; Email: ihamachi@sbchem.kyoto-u.ac.jp

Authors

Taro Hiroi – *Department of Synthetic Chemistry and Biological Chemistry, Graduate School of Engineering, Kyoto University, Katsura, Nishikyo-ku, Kyoto 615-8510, Japan*

Yuriki Ikuta – *Department of Synthetic Chemistry and Biological Chemistry, Graduate School of Engineering, Kyoto University, Katsura, Nishikyo-ku, Kyoto 615-8510, Japan*

Yuchong Liu – *Department of Synthetic Chemistry and Biological Chemistry, Graduate School of Engineering, Kyoto University, Katsura, Nishikyo-ku, Kyoto 615-8510, Japan*

Author contribution

R.K. and I.H. designed the work. R.K. conducted all of the experiments and analyzed the data. T.H. found temperature-dependent phase transition of the coacervate. Y.I. synthesized PEG_9-FW-OtBu and PEG_9-FL-OtBu. Y.L. synthesized PEG_9- and PEG_2-FF-OtBu. R.K. and I.H. wrote the manuscript.

Acknowledgements

We appreciate Dr. Fumiyoshi Ishidate (iCeMS Analysis Center, Kyoto University) for fruitful discussion about Airyscan imaging. This work was supported by a Grant-in-Aid for Scientific Research on Innovative Areas “Chemistry for Multimolecular Crowding Biosystems” (JSPS KAKENHI Grant JP17H06348), the Japan Science and Technology Agency (JST) ERATO Grant Number JPMJER1802 to I.H., and by a Grant-in-Aid for Young Scientists (JSPS KAKENHI Grant JP20K15400) and a Grant-in-Aid for Scientific Research (B) (JSPS KAKENHI Grant JP22H02195) to R.K. A part of this work was supported by “Advanced Research Infrastructure for Materials and Nanotechnology in Japan (ARIM)” of the Ministry of Education, Culture, Sports, Science and Technology (MEXT) Grant Number JPMXP1222KT0030. We thank Frank Kitching, MSc., from Edanz (https://jp.edanz.com/ac) for editing a draft of this manuscript.

Competing interests

The authors declare no competing interests.

References

(1) de Jong, H. G. B.; Kruyt, H. R. Coacervation (Partial Miscibility in Colloid Systems). *Proc. K. Ned. Akad. Wet.* **1929**, *32*, 849–856.

(2) Shin, Y.; Brangwynne, C. P. Liquid Phase Condensation in Cell Physiology and Disease. *Science* **2017**, *357*, eaaf4382.

(3) Aumiller, W. M., Jr; Keating, C. D. Experimental Models for Dynamic Compartmentalization of Biomolecules in Liquid Organelles: Reversible Formation and Partitioning in Aqueous Biphasic Systems. *Adv. Colloid Interface Sci.* **2017**, *239*, 75–87.

(4) Kuroyanagi, S.; Shimada, N.; Fujii, S.; Furuta, T.; Harada, A.; Sakurai, K.; Maruyama, A. Highly Ordered Polypeptide with UCST Phase Separation Behavior. *J. Am. Chem. Soc.* **2019**, *141*, 1261–1268.

(5) Sato, Y.; Sakamoto, T.; Takinoue, M. Sequence-Based Engineering of Dynamic Functions of Micrometer-Sized DNA Droplets. *Sci. Adv.* **2020**, *6*, eaba3471.

(6) Scott, W. A.; Gharakhanian, E. G.; Bell, A. G.; Evans, D.; Barun, E.; Houk, K. N.; Deming, T. J. Active Controlled and Tunable Coacervation Using Side-Chain Functional α-Helical Homopolypeptides. *J. Am. Chem. Soc.* **2021**, *143*, 18196–18203.

(7) Niu, J.; Qiu, C.; Abbott, N. L.; Gellman, S. H. Formation of versus Recruitment to RNA-Rich Condensates: Controlling Effects Exerted by Peptide Side Chain Identity. *J. Am. Chem. Soc.* **2022**, *144*, 10386–10395.

(8) Deepankumar, K.; Guo, Q.; Mohanram, H.; Lim, J.; Mu, Y.; Pervushin, K.; Yu, J.; Miserez, A. Liquid-Liquid Phase Separation of the Green Mussel Adhesive Protein Pvfp-5 Is Regulated by the Post-Translated Dopa Amino Acid. *Adv. Mater.* **2022**, *34*, e2103828.

(9) Jain, A.; Kassem, S.; Fisher, R. S.; Wang, B.; Li, T.-D.; Wang, T.; He, Y.; Elbaum-Garfinkle, S.; Ulijn, R. V. Connected Peptide Modules Enable Controlled Co-Existence of Self-Assembled Fibers Inside Liquid Condensates. *J. Am. Chem. Soc.* **2022**, *144*, 15002–15007.

(10) Tsuruta, M.; Torii, T.; Kohata, K.; Kawauchi, K.; Tateishi-Karimata, H.; Sugimoto, N.; Miyoshi, D. Controlling Liquid-Liquid Phase Separation of G-Quadruplex-Forming RNAs in a Sequence-Specific Manner. *Chem. Commun.* **2022**, *58*, 12931–12934.

(11) Obayashi, H.; Wakabayashi, R.; Kamiya, N.; Goto, M. Supramolecular Localization in Liquid-Liquid Phase Separation and Protein Recruitment in Confined Droplets. *Chem. Commun.* **2023**, *59*, 414–417.

(12) Oparin, A. I. Evolution of the Concepts of the Origin of Life. *Orig. Life* **1976**, *7*, 3–8.

(13) Szostak, J. W.; Bartel, D. P.; Luisi, P. L. Synthesizing Life. *Nature* **2001**, *409*, 387–390.

(14) Slootbeek, A. D.; van Haren, M. H. I.; Smokers, I. B. A.; Spruijt, E. Growth, Replication and Division Enable Evolution of Coacervate Protocells. *Chem. Commun.* **2022**, *58*, 11183–11200.
(15) Cook, A. B.; Novosedlik, S.; van Hest, J. C. M. Complex Coacervate Materials as Artificial Cells. *Acc. Mater. Res.* **2023**, *4*, 287–298.
(16) Koga, S.; Williams, D. S.; Perriman, A. W.; Mann, S. Peptide-Nucleotide Microdroplets as a Step towards a Membrane-Free Protocell Model. *Nat. Chem.* **2011**, *3*, 720–724.
(17) Andes-Koback, M.; Keating, C. D. Complete Budding and Asymmetric Division of Primitive Model Cells to Produce Daughter Vesicles with Different Interior and Membrane Compositions. *J. Am. Chem. Soc.* **2011**, *133*, 9545–9555.
(18) Dora Tang, T.-Y.; Rohaida Che Hak, C.; Thompson, A. J.; Kuimova, M. K.; Williams, D. S.; Perriman, A. W.; Mann, S. Fatty Acid Membrane Assembly on Coacervate Microdroplets as a Step towards a Hybrid Protocell Model. *Nat. Chem.* **2014**, *6*, 527–533.
(19) Aumiller, W. M., Jr; Keating, C. D. Phosphorylation-Mediated RNA/Peptide Complex Coacervation as a Model for Intracellular Liquid Organelles. *Nat. Chem.* **2016**, *8*, 129–137.
(20) Mason, A. F.; Buddingh', B. C.; Williams, D. S.; van Hest, J. C. M. Hierarchical Self-Assembly of a Copolymer-Stabilized Coacervate Protocell. *J. Am. Chem. Soc.* **2017**, *139*, 17309–17312.
(21) Drobot, B.; Iglesias-Artola, J. M.; Le Vay, K.; Mayr, V.; Kar, M.; Kreysing, M.; Mutschler, H.; Tang, T.-Y. D. Compartmentalised RNA Catalysis in Membrane-Free Coacervate Protocells. *Nat. Commun.* **2018**, *9*, 3643.
(22) Deshpande, S.; Brandenburg, F.; Lau, A.; Last, M. G. F.; Spoelstra, W. K.; Reese, L.; Wunnava, S.; Dogterom, M.; Dekker, C. Spatiotemporal Control of Coacervate Formation within Liposomes. *Nat. Commun.* **2019**, *10*, 1800.
(23) Donau, C.; Späth, F.; Sosson, M.; Kriebisch, B. A. K.; Schnitter, F.; Tena-Solsona, M.; Kang, H.-S.; Salibi, E.; Sattler, M.; Mutschler, H.; Boekhoven, J. Active Coacervate Droplets as a Model for Membraneless Organelles and Protocells. *Nat. Commun.* **2020**, *11*, 5167.
(24) Matsuo, M.; Kurihara, K. Proliferating Coacervate Droplets as the Missing Link between Chemistry and Biology in the Origins of Life. *Nat. Commun.* **2021**, *12*, 5487.
(25) Mu, W.; Ji, Z.; Zhou, M.; Wu, J.; Lin, Y.; Qiao, Y. Membrane-Confined Liquid-Liquid Phase Separation toward Artificial Organelles. *Sci. Adv.* **2021**, *7*, eabf9000.
(26) Ianeselli, A.; Tetiker, D.; Stein, J.; Kühnlein, A.; Mast, C. B.; Braun, D.; Dora Tang, T.-Y. Non-Equilibrium Conditions inside Rock Pores Drive Fission, Maintenance and Selection of Coacervate Protocells. *Nat. Chem.* **2022**, *14*, 32–39.

(27) Iglesias-Artola, J. M.; Drobot, B.; Kar, M.; Fritsch, A. W.; Mutschler, H.; Dora Tang, T.-Y.; Kreysing, M. Charge-Density Reduction Promotes Ribozyme Activity in RNA-Peptide Coacervates via RNA Fluidization and Magnesium Partitioning. *Nat. Chem.* **2022**, *14*, 407–416.

(28) Yin, Z.; Tian, L.; Patil, A. J.; Li, M.; Mann, S. Spontaneous Membranization in a Silk-Based Coacervate Protocell Model. *Angew. Chem. Int. Ed.* **2022**, *61*, e202202302.

(29) Xu, C.; Martin, N.; Li, M.; Mann, S. Living Material Assembly of Bacteriogenic Protocells. *Nature* **2022**, *609*, 1029–1037.

(30) Jho, Y.; Yoo, H. Y.; Lin, Y.; Han, S.; Hwang, D. S. Molecular and Structural Basis of Low Interfacial Energy of Complex Coacervates in Water. *Adv. Colloid Interface Sci.* **2017**, *239*, 61–73.

(31) Strey, R.; Jahn, W.; Porte, G.; Bassereau, P. Freeze Fracture Electron Microscopy of Dilute Lamellar and Anomalous Isotropic (L_3) Phases. *Langmuir* **1990**, *6*, 1635–1639.

(32) Hoffmann, H.; Thunig, C.; Munkert, U.; Meyer, H. W.; Richter, W. From Vesicles to the L_3 (Sponge) Phase in Alkyldimethylamine Oxide/Heptanol Systems. *Langmuir* **1992**, *8*, 2629–2638.

(33) Menger, F. M.; Peresypkin, A. V.; Caran, K. L.; Apkarian, R. P. A Sponge Morphology in an Elementary Coacervate. *Langmuir* **2000**, *16*, 9113–9116.

(34) Imura, T.; Yanagishita, H.; Kitamoto, D. Coacervate Formation from Natural Glycolipid: One Acetyl Group on the Headgroup Triggers Coacervate-to-Vesicle Transition. *J. Am. Chem. Soc.* **2004**, *126*, 10804–10805.

(35) Wibowo, A.; Osada, K.; Matsuda, H.; Anraku, Y.; Hirose, H.; Kishimura, A.; Kataoka, K. Morphology Control in Water of Polyion Complex Nanoarchitectures of Double-Hydrophilic Charged Block Copolymers through Composition Tuning and Thermal Treatment. *Macromolecules* **2014**, *47*, 3086–3092.

(36) Higashiguchi, K.; Taira, G.; Kitai, J.-I.; Hirose, T.; Matsuda, K. Photoinduced Macroscopic Morphological Transformation of an Amphiphilic Diarylethene Assembly: Reversible Dynamic Motion. *J. Am. Chem. Soc.* **2015**, *137*, 2722–2729.

(37) Kim, S.; Huang, J.; Lee, Y.; Dutta, S.; Yoo, H. Y.; Jung, Y. M.; Jho, Y.; Zeng, H.; Hwang, D. S. Complexation and Coacervation of Like-Charged Polyelectrolytes Inspired by Mussels. *Proc. Natl. Acad. Sci. U. S. A.* **2016**, *113*, E847-53.

(38) Bhattacharya, A.; Niederholtmeyer, H.; Podolsky, K. A.; Bhattacharya, R.; Song, J.-J.; Brea, R. J.; Tsai, C.-H.; Sinha, S. K.; Devaraj, N. K. Lipid Sponge Droplets as Programmable Synthetic

Organelles. *Proc. Natl. Acad. Sci. U. S. A.* **2020**, *117*, 18206–18215.
(39) Sing, C. E.; Perry, S. L. Recent Progress in the Science of Complex Coacervation. *Soft Matter* **2020**, *16*, 2885–2914.
(40) Kayitmazer, A. B.; Strand, S. P.; Tribet, C.; Jaeger, W.; Dubin, P. L. Effect of Polyelectrolyte Structure on Protein-Polyelectrolyte Coacervates: Coacervates of Bovine Serum Albumin with Poly(Diallyldimethylammonium Chloride) versus Chitosan. *Biomacromolecules* **2007**, *8*, 3568–3577.
(41) Spruijt, E.; Westphal, A. H.; Borst, J. W.; Cohen Stuart, M. A.; van der Gucht, J. Binodal Compositions of Polyelectrolyte Complexes. *Macromolecules* **2010**, *43*, 6476–6484.
(42) Marciel, A. B.; Srivastava, S.; Tirrell, M. V. Structure and Rheology of Polyelectrolyte Complex Coacervates. *Soft Matter* **2018**, *14*, 2454–2464.
(43) Carl, N.; Müller, W.; Schweins, R.; Huber, K. Controlling Self-Assembly with Light and Temperature. *Langmuir* **2020**, *36*, 223–231.
(44) Fares, H. M.; Marras, A. E.; Ting, J. M.; Tirrell, M. V.; Keating, C. D. Impact of Wet-Dry Cycling on the Phase Behavior and Compartmentalization Properties of Complex Coacervates. *Nat. Commun.* **2020**, *11*, 5423.
(45) Le Ferrand, H.; Duchamp, M.; Gabryelczyk, B.; Cai, H.; Miserez, A. Time-Resolved Observations of Liquid-Liquid Phase Separation at the Nanoscale Using in Situ Liquid Transmission Electron Microscopy. *J. Am. Chem. Soc.* **2019**, *141*, 7202–7210.
(46) Ianiro, A.; Wu, H.; van Rijt, M. M. J.; Vena, M. P.; Keizer, A. D. A.; Esteves, A. C. C.; Tuinier, R.; Friedrich, H.; Sommerdijk, N. A. J. M.; Patterson, J. P. Liquid-Liquid Phase Separation during Amphiphilic Self-Assembly. *Nat. Chem.* **2019**, *11*, 320–328.
(47) Kubota, R.; Tanaka, W.; Hamachi, I. Microscopic Imaging Techniques for Molecular Assemblies: Electron, Atomic Force, and Confocal Microscopies. *Chem. Rev.* **2021**, *121*, 14281–14347.
(48) Berry, J.; Brangwynne, C. P.; Haataja, M. Physical Principles of Intracellular Organization via Active and Passive Phase Transitions. *Rep. Prog. Phys.* **2018**, *81*, 046601.
(49) Linsenmeier, M.; Kopp, M. R. G.; Grigolato, F.; Emmanoulidis, L.; Liu, D.; Zürcher, D.; Hondele, M.; Weis, K.; Capasso Palmiero, U.; Arosio, P. Dynamics of Synthetic Membraneless Organelles in Microfluidic Droplets. *Angew. Chem. Int. Ed.* **2019**, *58*, 14489–14494.
(50) Nakashima, K. K.; van Haren, M. H. I.; André, A. A. M.; Robu, I.; Spruijt, E. Active Coacervate Droplets Are Protocells That Grow and Resist Ostwald Ripening. *Nat. Commun.* **2021**, *12*, 3819.

(51) Bergmann, A. M.; Donau, C.; Späth, F.; Jahnke, K.; Göpfrich, K.; Boekhoven, J. Evolution and Single-Droplet Analysis of Fuel-Driven Compartments by Droplet-Based Microfluidics. *Angew. Chem. Int. Ed.* **2022**, *61*, e202203928.
(52) Kubota, R.; Torigoe, S.; Hamachi, I. Temporal Stimulus Patterns Drive Differentiation of a Synthetic Dipeptide-Based Coacervate. *J. Am. Chem. Soc.* **2022**, *144*, 15155–15164.
(53) Frenkel-Pinter, M.; Samanta, M.; Ashkenasy, G.; Leman, L. J. Prebiotic Peptides: Molecular Hubs in the Origin of Life. *Chem. Rev.* **2020**, *120*, 4707–4765.
(54) Abbas, M.; Lipiński, W. P.; Wang, J.; Spruijt, E. Peptide-Based Coacervates as Biomimetic Protocells. *Chem. Soc. Rev.* **2021**, *50*, 3690–3705.
(55) Sheehan, F.; Sementa, D.; Jain, A.; Kumar, M.; Tayarani-Najjaran, M.; Kroiss, D.; Ulijn, R. V. Peptide-Based Supramolecular Systems Chemistry. *Chem. Rev.* **2021**, *121*, 13869–13914.
(56) Reches, M.; Gazit, E. Casting Metal Nanowires within Discrete Self-Assembled Peptide Nanotubes. *Science* **2003**, *300*, 625–627.
(57) Yang, Z.; Liang, G.; Wang, L.; Xu, B. Using a Kinase/Phosphatase Switch to Regulate a Supramolecular Hydrogel and Forming the Supramolecular Hydrogel in Vivo. *J. Am. Chem. Soc.* **2006**, *128*, 3038–3043.
(58) Ikeda, M.; Tanida, T.; Yoshii, T.; Hamachi, I. Rational Molecular Design of Stimulus-Responsive Supramolecular Hydrogels Based on Dipeptides. *Adv. Mater.* **2011**, *23*, 2819–2822.
(59) Yuan, C.; Levin, A.; Chen, W.; Xing, R.; Zou, Q.; Herling, T. W.; Challa, P. K.; Knowles, T. P. J.; Yan, X. Nucleation and Growth of Amino Acid and Peptide Supramolecular Polymers through Liquid-Liquid Phase Separation. *Angew. Chem. Int. Ed.* **2019**, *58*, 18116–18123.
(60) Abbas, M.; Lipiński, W. P.; Nakashima, K. K.; Huck, W. T. S.; Spruijt, E. A Short Peptide Synthon for Liquid-Liquid Phase Separation. *Nat. Chem.* **2021**, *13*, 1046–1054.
(61) Tang, Y.; Bera, S.; Yao, Y.; Zeng, J.; Lao, Z.; Dong, X.; Gazit, E.; Wei, G. Prediction and Characterization of Liquid-Liquid Phase Separation of Minimalistic Peptides. *Cell Rep. Phys. Sci.* **2021**, *2*, 100579.
(62) Kunishima, M.; Kawachi, C.; Hioki, K.; Terao, K.; Tani, S. Formation of Carboxamides by Direct Condensation of Carboxylic Acids and Amines in Alcohols Using a New Alcohol- and Water-Soluble Condensing Agent: DMT-MM. *Tetrahedron* **2001**, *57*, 1551–1558.
(63) Fisher, R. S.; Elbaum-Garfinkle, S. Tunable Multiphase Dynamics of Arginine and Lysine Liquid Condensates. *Nat. Commun.* **2020**, *11*, 4628.
(64) Saeki, S.; Kuwahara, N.; Nakata, M.; Kaneko, M. Upper and Lower Critical Solution Temperatures in Poly (Ethylene Glycol) Solutions. *Polymer* **1976**, *17*, 685–689.

(65) Alshareedah, I.; Moosa, M. M.; Raju, M.; Potoyan, D. A.; Banerjee, P. R. Phase Transition of RNA–protein Complexes into Ordered Hollow Condensates. *Proc. Natl. Acad. Sci. U. S. A.* **2020**, *117*, 15650–15658.

(66) Yin, Y.; Niu, L.; Zhu, X.; Zhao, M.; Zhang, Z.; Mann, S.; Liang, D. Non-Equilibrium Behaviour in Coacervate-Based Protocells under Electric-Field-Induced Excitation. *Nat. Commun.* **2016**, *7*, 10658.

(67) Banerjee, P. R.; Milin, A. N.; Moosa, M. M.; Onuchic, P. L.; Deniz, A. A. Reentrant Phase Transition Drives Dynamic Substructure Formation in Ribonucleoprotein Droplets. *Angew. Chem. Int. Ed.* **2017**, *56*, 11354–11359.

(68) Saleh, O. A.; Jeon, B.-J.; Liedl, T. Enzymatic Degradation of Liquid Droplets of DNA Is Modulated near the Phase Boundary. *Proc. Natl. Acad. Sci. U. S. A.* **2020**, *117*, 16160–16166.

(69) Moreau, N. G.; Martin, N.; Gobbo, P.; Tang, T.-Y. D.; Mann, S. Spontaneous Membrane-Less Multi-Compartmentalization via Aqueous Two-Phase Separation in Complex Coacervate Micro-Droplets. *Chem. Commun.* **2020**, *56*, 12717–12720.

(70) Donau, C.; Späth, F.; Stasi, M.; Bergmann, A. M.; Boekhoven, J. Phase Transitions in Chemically Fueled, Multiphase Complex Coacervate Droplets. *Angew. Chem. Int. Ed.* **2022**, e202211905.

(71) Erkamp, N. A.; Sneideris, T.; Ausserwöger, H.; Qian, D.; Qamar, S.; Nixon-Abell, J.; St George-Hyslop, P.; Schmit, J. D.; Weitz, D. A.; Knowles, T. P. J. Spatially Non-Uniform Condensates Emerge from Dynamically Arrested Phase Separation. *Nat. Commun.* **2023**, *14*, 684.

(72) Gao, N.; Xu, C.; Yin, Z.; Li, M.; Mann, S. Triggerable Protocell Capture in Nanoparticle-Caged Coacervate Microdroplets. *J. Am. Chem. Soc.* **2022**, *144*, 3855–3862.

(73) Oana, H.; Kishimura, A.; Yonehara, K.; Yamasaki, Y.; Washizu, M.; Kataoka, K. Spontaneous Formation of Giant Unilamellar Vesicles from Microdroplets of a Polyion Complex by Thermally Induced Phase Separation. *Angew. Chem. Int. Ed.* **2009**, *48*, 4613–4616.

(74) Jang, Y.; Hsieh, M.-C.; Dautel, D.; Guo, S.; Grover, M. A.; Champion, J. A. Understanding the Coacervate-to-Vesicle Transition of Globular Fusion Proteins to Engineer Protein Vesicle Size and Membrane Heterogeneity. *Biomacromolecules* **2019**, *20*, 3494–3503.

(75) Dautel, D. R.; Champion, J. A. Protein Vesicles Self-Assembled from Functional Globular Proteins with Different Charge and Size. *Biomacromolecules* **2021**, *22*, 116–125.

(76) Feric, M.; Vaidya, N.; Harmon, T. S.; Mitrea, D. M.; Zhu, L.; Richardson, T. M.; Kriwacki, R. W.; Pappu, R. V.; Brangwynne, C. P. Coexisting Liquid Phases Underlie Nucleolar

Subcompartments. *Cell* **2016**, *165*, 1686–1697.
(77) Lafontaine, D. L. J.; Riback, J. A.; Bascetin, R.; Brangwynne, C. P. The Nucleolus as a Multiphase Liquid Condensate. *Nat. Rev. Mol. Cell Biol.* **2021**, *22*, 165–182.
(78) Jain, S.; Wheeler, J. R.; Walters, R. W.; Agrawal, A.; Barsic, A.; Parker, R. ATPase-Modulated Stress Granules Contain a Diverse Proteome and Substructure. *Cell* **2016**, *164*, 487–498.
(79) Simon, J. R.; Carroll, N. J.; Rubinstein, M.; Chilkoti, A.; López, G. P. Programming Molecular Self-Assembly of Intrinsically Disordered Proteins Containing Sequences of Low Complexity. *Nat. Chem.* **2017**, *9*, 509–515.
(80) Chen, Y.; Yuan, M.; Zhang, Y.; Liu, S.; Yang, X.; Wang, K.; Liu, J. Construction of Coacervate-in-Coacervate Multi-Compartment Protocells for Spatial Organization of Enzymatic Reactions. *Chem. Sci.* **2020**, *11*, 8617–8625.
(81) Lu, T.; Spruijt, E. Multiphase Complex Coacervate Droplets. *J. Am. Chem. Soc.* **2020**, *142*, 2905–2914.
(82) Mountain, G. A.; Keating, C. D. Formation of Multiphase Complex Coacervates and Partitioning of Biomolecules within Them. *Biomacromolecules* **2020**, *21*, 630–640.
(83) Karoui, H.; Seck, M. J.; Martin, N. Self-Programmed Enzyme Phase Separation and Multiphase Coacervate Droplet Organization. *Chem. Sci.* **2021**, *12*, 2794–2802.
(84) Kaur, T.; Raju, M.; Alshareedah, I.; Davis, R. B.; Potoyan, D. A.; Banerjee, P. R. Sequence-Encoded and Composition-Dependent Protein-RNA Interactions Control Multiphasic Condensate Morphologies. *Nat. Commun.* **2021**, *12*, 872.
(85) Choi, S.; Meyer, M. O.; Bevilacqua, P. C.; Keating, C. D. Phase-Specific RNA Accumulation and Duplex Thermodynamics in Multiphase Coacervate Models for Membraneless Organelles. *Nat. Chem.* **2022**, *14*, 1110–1117.

1 **TOC Graphic**

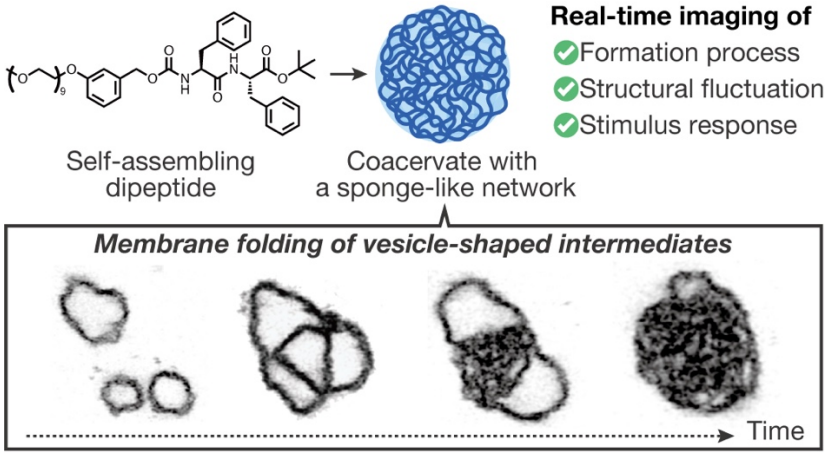

2

3